

AuViRe: Audio-visual Speech Representation Reconstruction for Deepfake Temporal Localization

Christos Koutlis

Information Technologies Institute @ CERTH
Thessaloniki, Greece

ckoutlis@iti.gr

Symeon Papadopoulos

Information Technologies Institute @ CERTH
Thessaloniki, Greece

papadop@iti.gr

Abstract

With the rapid advancement of sophisticated synthetic audio-visual content, e.g., for subtle malicious manipulations, ensuring the integrity of digital media has become paramount. This work presents a novel approach to temporal localization of deepfakes by leveraging Audio-Visual Speech Representation Reconstruction (AuViRe). Specifically, our approach reconstructs speech representations from one modality (e.g., lip movements) based on the other (e.g., audio waveform). Cross-modal reconstruction is significantly more challenging in manipulated video segments, leading to amplified discrepancies, thereby providing robust discriminative cues for precise temporal forgery localization. AuViRe outperforms the state of the art by +8.9 AP@0.95 on LAV-DF, +9.6 AP@0.5 on AV-Deepfake1M, and +5.1 AUC on an in-the-wild experiment. Code available at <https://github.com/mevert-team/auvire>.

1. Introduction

The advancement of generative AI has led to the rise of highly realistic synthetic media, often referred to as deepfakes [27]. These audio-visual manipulations threaten digital integrity, as they are designed to be perceptually convincing and capable of deceiving both humans and automated systems. This deceptive capacity fuels misinformation, erodes public trust, and carries significant societal and security risks. Ensuring the integrity of audio-visual content has become a critical challenge, driving the need for robust deepfake detection and temporal localization solutions.

While significant progress has been made in deepfake detection, accurately identifying and temporally localizing manipulations in audio-visual content remains a substantial challenge. Existing methods [8, 9, 18, 19, 21, 25, 31, 34–36], primarily focus on coarse-grained video classification instead of temporal forgery localization, while neglecting to

also leverage the subtle cross-modal inconsistencies that are crucial for fine-grained temporal localization. In contrast, spatial forgery localization, being out of this work’s scope, has been widely explored [32, 40]. Crucially, most state of the art multimodal deepfake detectors [7, 10], directly process the raw audio-visual signal instead of utilizing high-level features extracted by large models, which renders them prone to overfitting and less robust to content distortions, or utilize general purpose feature extractors [6, 39] limiting their representational capacity.

AuViRe addresses these limitations by explicitly modeling cross-modal discrepancies in speech representations. It leverages pre-trained speech-related feature extractors [30] for both visual and audio modalities, providing highly relevant and robust cues for detecting forged speech. Designed for Temporal Forgery Localization (TFL), our approach enables both fine-grained (frame-level) and coarse-grained (video-level) predictions rendering it also suitable for Deepfake Detection (DFD). Specifically, the proposed architecture first independently extracts visual and audio speech-related features. A representation reconstruction module then predicts visual speech representations from audio, complemented by unimodal (audio-audio and visual-visual) reconstructions. Finally, a reconstruction-discrepancy encoder processes these reconstruction errors to identify forgery features. AuViRe outperforms the state of the art by +8.9 AP@0.95 on LAV-DF [7], +9.6 AP@0.5 on AV-Deepfake1M [5] benchmarks. In addition, we provide a real-world implementation accounting for the presence of both visual and audio streams, large video lengths, and talking human presence, yielding +5.1 AUC on in-the-wild experiments. Our main contributions are:

1. The proposed AuViRe architecture, a novel framework for audio-visual deepfake temporal localization based on cross-modal reconstruction discrepancy modeling.
2. An extensive evaluation on established benchmarks (LAV-DF, AV-Deepfake1M) achieving state of the art performance on both TFL and DFD.

3. A real-world evaluation of AuViRe, demonstrating strong performance in the wild.

2. Related Work

Video Deepfake Detection. Pertinent methods focus on spatio-temporal inconsistencies [9, 18], analyze frequency domain artifacts [14, 19], or use a multi-attentional approach [40]. Approaches like SBI [31] and SLADD [8] use sophisticated augmentations to train on diverse synthetic forgeries, while SeeABLE [21] reframes the problem as one-class anomaly detection. TALL transforms video clips into thumbnails, efficiently capturing spatio-temporal inconsistencies. Datasets like FaceForensics++ [29], CelebDF [23], and DFDC [13] have been instrumental in advancing these techniques. While achieving notable success in controlled environments, these video-level detectors struggle under partial multimodal forgeries.

Multimodal Deepfake Detection. The emergence of audio-visual deepfakes, where both visual and auditory streams are potentially manipulated, has necessitated the development of multimodal detection approaches. These methods look for inconsistencies across modalities, as maintaining perfect synchronization and consistency between visual and audio streams is still challenging for deepfake generators. Existing multimodal detectors such as those by Chugh et al. [10] and Cai et al. [7], typically concatenate or employ attention mechanisms to combine features extracted from raw audio and visual signals. However, directly processing raw signals can lead to overfitting to specific artifacts, reduced robustness to real-world distortions, and may not capture high-level semantic inconsistencies effectively. Some approaches use pre-extracted features, but rely on general-purpose encoders [6, 39] lacking the capacity for speech-related understanding, which is crucial for the task.

Temporal Deepfake Localization. Beyond binary classification (real vs. fake), the temporal localization of manipulated segments is important for forensic analysis, as it enables more fine-grained and transparent decisions about suspicious content. Recent works address this challenge, proposing methods that analyze spatio-temporal cross-modal consistency [6, 39]. While these methods constitute an important step towards fine-grained deepfake analysis, they utilize general purpose feature extractors limiting their representational capacity. Our work addresses this by modeling frame-level cross-modal discrepancies in the speech latent space. DiMoDif [20] also considers speech-related features for cross-modal incongruity identification; however, our framework is fundamentally different leveraging cross-modal *reconstruction discrepancy* instead of plain features encoding and comparison.

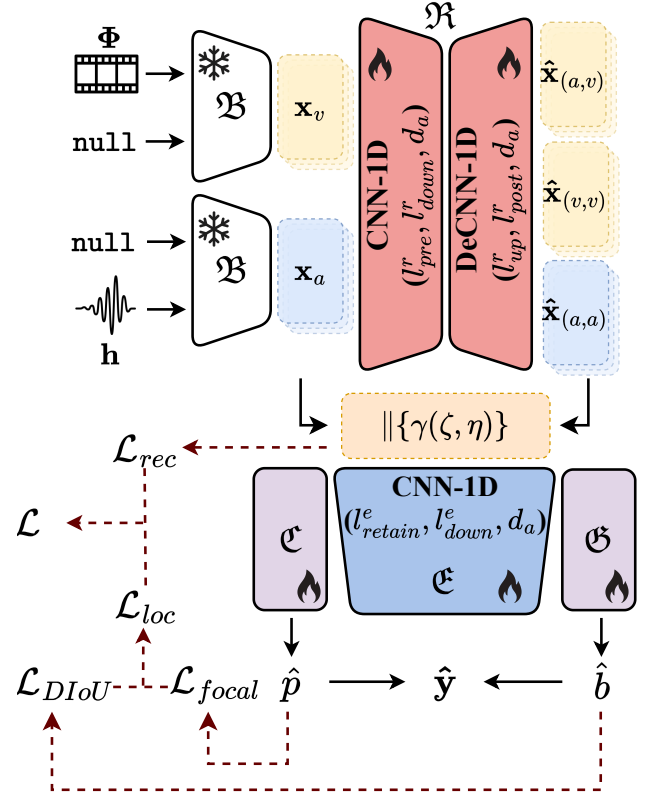


Figure 1. The proposed AuViRe architecture.

3. Methodology

In this section we elaborate on the proposed framework AuViRe, which is illustrated in Fig. 1.

3.1. Problem Formulation

Consider a dataset \mathcal{V} comprising pairs of video and ground truth (\mathbf{v}, \mathbf{y}) . Each input video \mathbf{v} has a duration of Δ seconds and consists of a visual stream $\Phi \in \mathbb{R}^{t \times h \times w \times c}$ and an audio stream $\mathbf{h} \in \mathbb{R}^{s \times n}$. Specifically, Φ contains t frames, each of size $h \times w \times c$, while \mathbf{h} contains s samples across n channels. The corresponding ground-truth annotation $\mathbf{y} \in \mathbb{R}^{t \times 3}$ is a concatenation of a per-frame manipulation target $p \in \{0, 1\}^t$ and manipulation boundary information $b \in [0, \Delta]^{t \times 2}$. For each frame $\tau \in [0, t]$, $p^\tau = 1$ indicates manipulation, and b^τ specifies the start and end times of the manipulated segment it belongs to, being valid for manipulated frames only. Our goal is to train a model $f(\mathbf{v}) \rightarrow \hat{\mathbf{y}}$ to temporally localize the manipulated parts of deepfake videos.

3.2. Visual and Audio Speech Representations

Our architecture first extracts visual $\mathbf{x}_v \in \mathbb{R}^{t \times d}$ and audio $\mathbf{x}_a \in \mathbb{R}^{t \times d}$ representations from a self-supervised

model [30]¹, \mathfrak{B} , primarily designed for speech recognition, to incorporate multimodal speech information in the processing pipeline. Specifically, the visual stream Φ and audio stream \mathbf{h} of the video are processed separately by the backbone model avoiding modality blending that could eliminate fake samples’ cross-modal discrepancies:

$$\mathbf{x}_v = \mathfrak{B}(\Phi, \text{null}), \quad \mathbf{x}_a = \mathfrak{B}(\text{null}, \mathbf{h}) \quad (1)$$

\mathfrak{B} is a self-supervised model that uses separate audio and visual encoders feeding into a transformer to learn audio-visual speech representations by iteratively clustering multimodal features and predicting masked segments. In our framework \mathfrak{B} is frozen during training.

3.3. Representation Reconstruction Module

The extracted representations $\mathbf{x}_v, \mathbf{x}_a$ are further processed by a reconstruction model, \mathfrak{R} , that utilizes them as input and target interchangeably. Its task is to predict the visual representation sequence based on the audio one as well as its visual-visual and audio-audio counterparts, namely:

$$\hat{\mathbf{x}}_{(a,v)} = \mathfrak{R}(\mathbf{x}_a), \quad \hat{\mathbf{x}}_{(v,v)} = \mathfrak{R}(\mathbf{x}_v), \quad \hat{\mathbf{x}}_{(a,a)} = \mathfrak{R}(\mathbf{x}_a) \quad (2)$$

with $\hat{\mathbf{x}}_{(\zeta,\eta)} \in \mathbb{R}^{t \times d}$, $\zeta, \eta \in \{a, v\}$, denoting the reconstruction of \mathbf{x}_η from \mathbf{x}_ζ . In general this process defines an easier objective when dealing with real samples that lack visual or audio artifacts. Thus, reconstruction discrepancies after subsequent processing should reveal manipulated video parts, if any. \mathfrak{R} comprises a pre-projection block of l_{pre}^r , d_a -dimensional, 1D convolutional layers with kernel size $\kappa = 3$ and stride $\sigma = 1$, a down-sampling encoder-block of l_{down}^r , d_a -dimensional, 1D convolutional layers ($\kappa = \kappa, \sigma = 2$), an up-sampling decoder-block of l_{up}^r , d_a -dimensional, 1D deconvolutional layers ($\kappa = \kappa, \sigma = 2$), and a post-projection block of $l_{post}^r - 1$, d_a -dimensional, and 1, d -dimensional, 1D convolutional layers ($\kappa = 3, \sigma = 1$). Convolutional and deconvolutional layers are followed by Layer Normalization (LN) [2] and ReLU.

3.4. Reconstruction-Discrepancy Encoder

The reconstruction-discrepancy encoder module is employed to identify forgery features by amplifying the reconstruction discrepancies during manipulated video parts. Its input $\mathbf{x} \in \mathbb{R}^{t \times d \times 3}$ preparation includes reconstruction-discrepancy computation, and concatenation (\parallel):

$$\mathbf{x} = \gamma(a, v) \parallel \gamma(v, v) \parallel \gamma(a, a) \quad (3)$$

where $\gamma(\zeta, \eta) = \hat{\mathbf{x}}_{(\zeta,\eta)} - \mathbf{x}_\eta$. Then, q -dimensional forgery-specific features $\mathbf{f} \in \mathbb{R}^{t \times l \times q}$ are produced by the reconstruction-discrepancy encoder model, \mathfrak{E} :

$$\mathbf{f} = \mathfrak{E}(\mathbf{x}) \quad (4)$$

¹We consider the AV-Hubert Base/LRS3/No-finetuning version from https://facebookresearch.github.io/av_hubert/.

implemented through a sequence of l_{retain}^e , d_a -dimensional, 1D convolutional layers ($\kappa = \kappa, \sigma = 1$) retaining timesteps t and a sequence of l_{down}^e , d_a -dimensional, 1D convolutional layers ($\kappa = \kappa, \sigma = 2$) of downsampled timesteps (i.e., $t/2^{\lambda_{down}}$, $\lambda_{down} = 1, \dots, l_{down}^e$), additionally incorporating a feature pyramid network on top of its l layers, with $l = l_{retain}^e + l_{down}^e$. Convolutional layers are followed by LN and ReLU.

3.5. Predictions

To obtain the temporal forgery localization predictions $\hat{\mathbf{y}} \in \mathbb{R}^{t \times l \times 3}$, our architecture uses a classification head \mathfrak{C} , for the manipulation detections \hat{p} per frame t , and a regression head \mathfrak{G} , for the manipulation boundaries \hat{b} if frame t lies within a manipulated video part, by processing the forgery features \mathbf{f} :

$$\hat{p} = \mathfrak{C}(\mathbf{f}), \quad \hat{b} = \mathfrak{G}(\mathbf{f}) \quad (5)$$

with $\hat{\mathbf{y}} = \hat{p} \parallel \hat{b}$, $\hat{p} \in \mathbb{R}^{t \times l}$, and $\hat{b} \in \mathbb{R}^{t \times l \times 2}$. \mathfrak{C} and \mathfrak{G} heads comprise 2, d_a -dimensional, and 1, d_{out} -dimensional, 1D convolutional layers ($\kappa = 3, \sigma = 1$) with $d_{out} = 1$ for \mathfrak{C} and $d_{out} = 2$ for \mathfrak{G} , each followed by LN and ReLU. Additionally, SoftNMS [4] is considered to enhance detection performance by re-weighting overlapping boundary \hat{b} predictions. Let $\mathcal{J} = \{(s_j, e_j, \rho_j)\}_{j=1}^M$ be the set of M predicted segments after applying SoftNMS, where s_j and e_j are the start and end times of the j -th segment, and ρ_j is its confidence score. Finally, since AuViRe is primarily trained on Temporal Forgery Localization (TFL) and not explicitly on binary deepfake detection, video-level predictions (\hat{y}) and targets (y) are post-processed as follows:

$$\hat{y} = \max_j \rho_j, \quad y = \bigvee_{\tau=1}^t p^\tau \quad (6)$$

This allows us to evaluate AuViRe on deepfake detection as an emergent property from its localization training.

3.6. Objective Function

To optimize our model, we consider a composite objective function accounting for manipulation detection and localization, as well as reconstruction-discrepancies minimization for real samples. Specifically, the focal loss \mathcal{L}_{focal} [24] is considered for per-frame manipulation detection, the DIOU loss \mathcal{L}_{DIOU} [41] is considered for manipulation localization, and a mean absolute error-based loss \mathcal{L}_{rec} is considered for reconstruction discrepancies minimization. The final loss \mathcal{L} is computed with Eq. (9), after computing

Eqs. (7) and (8).

$$\mathcal{L}_{loc} = \frac{1}{l} \sum_{\lambda} \sum_{\tau}^t \left(\mathcal{L}_{focal}(\hat{p}^{\tau, \lambda}, p^{\tau}) + p^{\tau} \cdot \mathcal{L}_{DIOU}(\hat{b}^{\tau, \lambda}, b^{\tau}) \right) / \sum_{\tau}^t p^{\tau} \quad (7)$$

$$\mathcal{L}_{rec} = \frac{\sum_{\tau=1}^t \gamma p^{\tau}}{t \cdot d} \sum_{\tau}^t \sum_{\delta}^d \sum_{\zeta, \eta \in \{a, v\}} |\hat{\mathbf{x}}_{\zeta, \eta} - \mathbf{x}_{\eta}| \quad (8)$$

with ζ, η the pairs that define Eq. (3).

$$\mathcal{L} = \frac{\mathcal{L}_{loc} + \mathcal{L}_{rec}}{2} \quad (9)$$

4. Experimental Setup

4.1. Datasets

With respect to controlled experiments we consider two popular Temporal Forgery Localization benchmarks, i.e., LAV-DF [6] and AV-Deepfake1M [5], which we also consider for video-level deepfake detection evaluation. LAV-DF contains 78,703 training, 31,501 validation, and 26,100 test samples. AV-Deepfake1M contains 746,180 training, 57,340 validation, and 343,240 test samples, the latter without released labels enabling evaluation only through Codabench². Additionally, we conduct a real-world analysis on a collection of 371 videos curated with the help of professional fact-checkers, 225 real and 146 manipulated, with median duration 1 minute (minimum: 10 sec, maximum: 11.3 minutes), spanning 39 languages³.

4.2. Implementation Details

We trained our method for 100 epochs using the Adam optimizer with an initial learning rate of 0.001 (reduced on plateau) and a batch size of 64. We implemented early stopping with a patience of 10, and checkpointing based on the sum of validation AP@{.} and AR@{.}. We used a maximum sequence length (t) of 512, zero-padding smaller sequences. Key architectural parameters included a kernel size (κ) of 15 and a model dimension (d_a) of 128. For the LAV-DF trained instance, the reconstruction model \mathfrak{R} layers were configured as $l_{pre}^r = 2$, $l_{down}^r = 3$, $l_{up}^r = 3$, and $l_{post}^r = 2$, while the reconstruction-discrepancy encoder model \mathfrak{E} layers were $l_{retain}^e = 2$ and $l_{down}^e = 2$. For the AV-Deepfake1M trained instance only $l_{down}^r, l_{up}^r, l_{retain}^e, l_{down}^e = 1$ deviate. We performed light tuning wrt $d_a \in \{32, 64, 128, 256\}$, $l_{down}^r, l_{up}^r \in \{1, 2, 3\}$, and $l_{retain}^e, l_{down}^e \in \{1, 2, 3\}$. Training was conducted on NVIDIA GeForce RTX 4090 GPUs.

²<https://deepfakes1m.github.io/2024/evaluation>

³Identified via <https://speechbrain.github.io/>

4.3. Real-world Application Implementation

The method implementation, as described in Sec. 3, is well-suited for evaluation under controlled laboratory settings on academic benchmarks. However, deploying it to real-world web videos presents a multifaceted challenge. To address this, we apply several practical adaptations: we verify the existence of both visual and audio streams, implement video chunking⁴ for long content to mitigate memory issues, ensure the presence of adequately sized⁵ and speaking individuals⁶, and apply the trained model only to relevant video segments of sufficient duration⁷ (henceforth referred to as `valid` and denoted $\beta = \cup_i \beta_i \subseteq [0, \Delta]$) to obtain meaningful predictions. Beyond these adaptations, several unaddressed factors frequently trigger false positive predictions for small and sparse video segments, even in real videos. These include variations in video quality (e.g., compression rate, audio noise) and the inherent characteristics of the training dataset, which contains only short-duration manipulations. To counter these issues and robustly score videos for manipulation in the wild, we propose two methods for aggregating model predictions:

- **Manipulation-fraction:** We define the manipulation-fraction score Ψ_m as the ratio of the total length of predicted manipulated segments to the total length of `valid` video segments β .

$$\Psi_m = \frac{\mu \left(\bigcup_j \{s_j, e_j\} \mid \rho_j > \theta \right)}{\mu \left(\bigcup_i \beta_i \right)} \quad (10)$$

For a probability threshold θ , with μ denoting the Lebesgue measure.

- **Sweep-like:** This method, inspired by the plane sweep algorithm of computational geometry domain [12], sorts all unique start s_j and end e_j points creating a sequence of event times $\iota_1 < \iota_2 < \dots < \iota_Q$. For each sub-segment $[\iota_k, \iota_{k+1})$, we calculate the average confidence score across overlapping predicted intervals. The Sweep-like score Ψ_s is then computed as the sum of these average scores, weighted by their respective durations:

$$\Psi_s = \sum_{k=1}^{Q-1} \left(\frac{\sum_j |s_j \leq \iota_k < e_j| \rho_j}{\Omega_k} \right) \cdot (\iota_{k+1} - \iota_k) \quad (11)$$

where $\Omega_k = |\{j \mid s_j \leq \iota_k < e_j\}|$ denotes the number of active intervals in the segment $[\iota_k, \iota_{k+1})$. This

⁴We consider 20 sec chunks.

⁵Minimum face size is 3% of frame area.

⁶After empirical validation, we consider a mouth as non-talking if $\|\mathbf{x}_v^{\tau-1} - \mathbf{x}_v^{\tau}\|_2 < 2$, for a frame τ .

⁷Minimum segment duration is 2 sec.

approach effectively integrates the confidence scores over time, naturally accounting for overlaps by averaging scores in regions of intersection.

4.4. Evaluation

We assess TFL performance using the standard $AP@{\cdot}$ and $AR@{\cdot}$ metrics. For Deepfake detection, we evaluate performance with the Area Under ROC Curve (AUC) and Average Precision (AP) metrics.

5. Results

5.1. Temporal Forgery Localization

AuViRe was trained for TFL using the LAV-DF and AV-Deepfake1M datasets. As detailed in Tabs. 1 and 2, our method outperforms state-of-the-art approaches across all metrics on both test sets. Specifically, on LAV-DF dataset, AuViRe shows a +8.9 absolute increase in terms of the challenging $AP@0.95$ metric, while maintaining strong performance on other metrics. On AV-Deepfake1M, AuViRe demonstrates significant improvements: +9.6 $AP@0.5$, +13.4 $AP@0.75$, +14.2 $AP@0.9$, +6.3 $AP@0.95$, +4.5 $AR@50$, +5.0 $AR@30$, +5.3 $AR@20$, +6.1 $AR@10$, and +7.2 $AR@5$. These results, particularly outperforming DiMoDif [20] (which also uses speech-related inputs), highlight the significant value of our representation reconstruction module in constructing and leveraging distinctive forgery features.

5.2. Video-level Deepfake Detection

Even though AuViRe is not trained for video-level deepfake detection, its frame-level outputs can be interpreted to provide this. Specifically, if the model does not localize any forgery, we consider it a non-detection. However, if any frame is detected as a deepfake, we interpret this as a positive deepfake detection for the video, as illustrated by Eq. (6). Tables 3 and 4 illustrate the performance of AuViRe along with competitive methods for video-level deepfake detection on LAV-DF and AV-Deepfake1M, respectively. On LAV-DF, AuViRe outperforms the previous state of the art, DiMoDif, achieving almost perfect performance, i.e., 99.94 AUC. On AV-Deepfake1M, AuViRe outperforms the state of the art by +3.5 AUC with very strong performance, i.e., 99.8 AUC.

5.3. Real-world Analysis

Table 5 showcases AuViRe’s performance on a collection of real-world videos sourced from social media. We observed a significant performance drop compared to our controlled experiments on academic benchmarks (75.5 AUC vs. 99.9 AUC). This highlights the inherent difficulty of detecting “in-the-wild” manipulations, which often encompass

diverse compression artifacts, varied lighting conditions, and subtle, sophisticated forgery techniques not typically present in curated datasets. Despite these challenges, our method outperforms existing state-of-the-art approaches, specifically DiMoDif and RealForensics, on the same real-world video set. This demonstrates AuViRe’s superior robustness and generalization capabilities in more realistic and uncontrolled environments. The manipulation-fraction variant Ψ_m performs better than the sweep-like variant Ψ_s , which is attributed to the fact that AuViRe’s output contains several noisy predictions with many $\rho_i < 0.01$, in this uncontrolled setting, that influence the sweep-like score. On the other hand, we set a threshold $\theta = 0.01$ for the manipulation-fraction method to overcome this. To assess the performance of the real-world implementation on academic benchmarks we sample 1000 videos from LAV-DF’s test set. AuViRe achieves strong performance with 84.5 AUC - 93.7 AP for Ψ_m , and 96.2 AUC - 98.6 AP for Ψ_s , indicating that the absence of noisy outputs favors the sweep-like approach. Finally, we assess performance per language in this set and present the top 5 in terms of count in Tab. 6.

5.3.1 Performance-drop factors

Given the definition of Ψ_m (Eq. (10)) as the fraction of manipulated video parts and the distribution of Ψ_m scores across real and fake samples (cf. Tab. 7), the performance drop is primarily attributed to false positives rather than false negatives. Specifically, only 8 out of 146 **fake** videos obtain a $\Psi_m < 23.27$, while 141 out of 225 **real** videos obtain a $\Psi_m > 23.27$. Fig. 2 presents indicative examples of clearly correctly ($\Psi_m < 12.64$) and erroneously

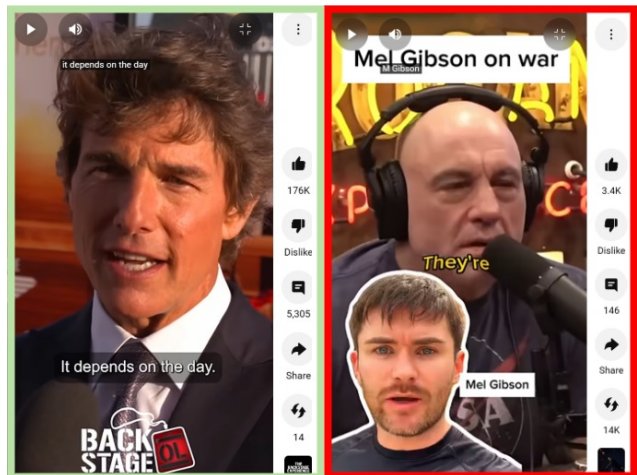


Figure 2. Examples of correctly (left; <https://www.youtube.com/shorts/xAPIjkhXF-0>) and erroneously (right; <https://www.youtube.com/shorts/D9mQGzG9dRk>) classified **real** samples.

Method	Modality	AP@0.5	AP@0.75	AP@0.95	AR@100	AR@50	AR@20	AR@10
MDS [10]	\mathcal{AV}	12.8	1.6	0.0	37.9	36.7	34.4	32.2
AVFusion [3]	\mathcal{AV}	65.4	23.9	0.1	63.0	59.3	54.8	52.1
ActionFormer [37]	\mathcal{V}	95.3	90.2	23.7	88.4	89.6	90.3	90.4
BA-TFD [7]	\mathcal{AV}	76.9	38.5	0.3	66.9	64.1	60.8	58.4
BA-TFD+ [6]	\mathcal{AV}	96.3	85.0	4.4	81.6	80.5	79.4	78.8
UMMAFormer [39]	\mathcal{AV}	<u>98.8</u>	<u>95.5</u>	<u>37.6</u>	92.4	92.5	92.5	<u>92.1</u>
DiMoDif [20]	\mathcal{AV}	95.5	87.9	20.6	<u>94.2</u>	<u>93.7</u>	<u>92.7</u>	91.4
AuViRe (ours)	\mathcal{AV}	98.9	96.0	46.5	94.9	94.6	94.0	93.3

Table 1. Temporal forgery localization results on LAV-DF [7]. Modality denotes the model’s input type with \mathcal{V} being visual and \mathcal{A} audio. **Bold** indicates best and underline second to best performance.

Method	Modality	AP@0.5	AP@0.75	AP@0.9	AP@0.95	AR@50	AR@30	AR@20	AR@10	AR@5
MesoInception4 [1]	\mathcal{V}	08.50	05.16	01.89	00.50	39.27	39.22	39.00	35.78	24.59
ActionFormer+VideoMAEv2 [33, 37]	\mathcal{V}	20.24	05.73	00.57	00.07	19.97	19.93	19.81	19.11	17.80
BA-TFD [7]	\mathcal{AV}	37.37	6.34	0.19	0.02	45.55	40.37	35.95	30.66	26.82
BA-TFD+ [6]	\mathcal{AV}	44.42	13.64	0.48	0.03	48.86	44.51	40.37	34.67	29.88
UMMAFormer [39]	\mathcal{AV}	51.64	28.07	7.65	1.58	44.07	43.93	43.45	42.09	40.27
DiMoDif [20]	\mathcal{AV}	<u>86.93</u>	<u>75.95</u>	<u>28.72</u>	<u>5.43</u>	<u>81.57</u>	<u>80.85</u>	<u>80.25</u>	<u>78.84</u>	<u>76.64</u>
AuViRe (ours)	\mathcal{AV}	96.5	89.3	42.9	11.7	86.0	85.8	85.5	84.9	83.8

Table 2. Temporal forgery localization results on AV-Deepfake1M [5]. Modality denotes the model’s input type with \mathcal{V} being visual and \mathcal{A} audio. **Bold** indicates best and underline second to best performance. *Reports validation performance.

Method	Modality	AUC
F ³ -Net [28]	\mathcal{V}	52.0
MDS [10]	\mathcal{AV}	82.8
EfficientViT [11]	\mathcal{V}	96.5
BA-TFD [7]	\mathcal{AV}	99.0
UMMAFormer [39]	\mathcal{AV}	99.8
DiMoDif [20]	\mathcal{AV}	<u>99.84</u>
AuViRe (ours)	\mathcal{AV}	99.94

Table 3. Video-level deepfake detection results on LAV-DF [7]. Modality denotes the model’s input type with \mathcal{V} being visual and \mathcal{A} audio. **Bold** indicates best and underline second to best performance.

Method	Modality	AUC
Video-LLaMA (13B) E5 [38]	\mathcal{AV}	50.7
LipForensics [17]	\mathcal{V}	51.6
Face X-Ray [22]	\mathcal{V}	61.5
MesoInception4 [1]	\mathcal{V}	50.1
SBI [31]	\mathcal{V}	65.8
MDS [10]	\mathcal{AV}	56.6
DiMoDif [20]	\mathcal{AV}	<u>96.3</u>
AuViRe (ours)	\mathcal{AV}	99.8

Table 4. Video-level deepfake detection results on AV-Deepfake1M [5]. Modality denotes the model’s input type with \mathcal{V} being visual and \mathcal{A} audio. **Bold** indicates best and underline second to best performance.

($\Psi_m > 62.04$) classified **real** samples. The left (correct) example, *in contrast to the right* (erroneous), is **free from mouth-occlusion**, contains **only one** clearly visible individual, has **no hard cuts**, and presents clear audio speech **without mix with music**; interestingly it exhibits some low-level background noise that does not affect the result. After visual inspection of all clearly correct ($\Psi_m < 12.64$) and erroneous ($\Psi_m > 62.04$) predictions for **real** samples we identified several underlying factors that potentially affect performance. Tab. 8 illustrates the corresponding fractions, clearly showing that significantly higher values are present in misclassified videos. The highest differences, in-

method	AUC	AP
DiMoDif [20]	61.6	55.7
RealForensics [16]	70.4	59.9
AuViRe (Ψ_m)	75.5	67.2
AuViRe (Ψ_s)	<u>71.0</u>	<u>62.3</u>

Table 5. Real-world performance.

dicating the most prominent factors of performance drop, are found for videos containing *long shots*, *multiple sub-*

Language	Videos (#)	Ψ_m		Ψ_s	
		AUC	AP	AUC	AP
English	282	77.9	64.4	73.6	60.0
Welsh	42	86.2	74.4	71.4	56.2
French	24	60.1	68.3	54.5	59.7
Greek	17	90.9	73.5	81.8	74.6
Spanish	16	86.7	94.2	88.3	94.8

Table 6. AuViRe’s real-world performance per language.

jects that talk during the course of the video, multi-subject frames, and non-English speech. In contrast, monochromatism, gender, mouth-occlusion, and race factors were found to be less significant. To mitigate these challenges, future work should focus on the inclusion of language-diverse training samples and more accurate isolation of each individual’s visuals and audio during inference.

5.4. Robustness

Fig. 3 compares the robustness of AuViRe against the next most competitive approach, DiMoDif. The evaluation was conducted on 1,000 unseen samples from the LAV-DF dataset, incorporating seven visual and four audio distortions, each applied across five intensity levels. Both models exhibit high robustness to most distortions, a quality

q	5	10	25	50	75	90
real	9.15	12.64	21.60	33.29	46.87	62.04
fake	23.27	27.55	38.38	53.28	72.22	84.21

Table 7. Percentiles of Ψ_m distribution in **real** vs. **fake** samples.

Table 8. Factors’ fractions for **real** videos obtaining correct (low Ψ_m) versus erroneous (high Ψ_m) predictions.

	Non-English Speech	Non-Native Accent	Speech/Music Mix
Corr. (Low Ψ_m)	13.04%	4.35%	17.39%
Err. (High Ψ_m)	34.78%	17.39%	26.09%
	Low Fidelity	Mono-chromatic	Long Shot
Corr. (Low Ψ_m)	0.00%	4.35%	4.35%
Err. (High Ψ_m)	13.04%	4.35%	43.48%
	Multiple Subjects	Multi-Subject Frames	Hard Cuts
Corr. (Low Ψ_m)	13.04%	0.00%	4.35%
Err. (High Ψ_m)	43.48%	30.43%	13.04%
	Mouth Occl.	Non-Caucasian Speaker	Female Speaker
Corr. (Low Ψ_m)	17.39%	13.04%	17.39%
Err. (High Ψ_m)	21.74%	21.74%	17.39%

partly attributed to the resilience of their underlying speech-related features. DiMoDif’s performance degrades most significantly under visual distortions, specifically Gaussian noise and video compression, and with the pitch shift audio distortion. In contrast, AuViRe remains resilient to these effects. Conversely, AuViRe maintains near-perfect robustness across all conditions except for Gaussian audio noise, where it experiences a more substantial performance drop than DiMoDif.

5.5. Ablation study

Tab. 9 reports ablation experiments on the LAV-DF dataset, investigating the loss composition (\mathcal{L} comp.), reconstruction-discrepancy encoder input (\mathcal{E} input), reconstruction-discrepancy operation ($\gamma(\zeta, \eta)$), backbone (\mathfrak{B}), and model type (\mathcal{M}). AuViRe’s original configuration includes $\{\mathcal{L}_{focal}, \mathcal{L}_{DIOU}, \mathcal{L}_{rec}\}$ for \mathcal{L} composition, $\{(a, v), (a, a), (v, v)\}$ for \mathcal{E} input, $(\hat{\mathbf{x}}_{(\zeta, \eta)} - \mathbf{x}_\eta)$ for $\gamma(\zeta, \eta)$, Shi et al. (2022) [30] for \mathfrak{B} , and CNN for \mathcal{M} . We also consider smooth L1 loss (\mathcal{L}_{s-L1}) [15] as an alternative to \mathcal{L}_{DIOU} for localization optimization, and video-level binary cross-entropy (\mathcal{L}_{det}) for auxiliary supervision. The proposed configuration achieves the highest $AP@{0.5, 0.75}$ scores and the best average rank. Immediate competitors involve slight modifications to \mathcal{E} ’s input. In contrast, significant modifications, e.g., using only $\{(v, v)\}$, lead to the worst performance highlighting the critical importance of cross-modal representation reconstruction. Limited variability is observed wrt loss composition though certain configurations show occasional deviations. Finally, using multiplication as discrepancy estimator, the backbone from Ma et al. [26], or Transformer⁸ model type yield suboptimal performance.

5.6. Computational Efficiency

In addition to achieving state of the art performance across both controlled and in-the-wild environments, AuViRe exhibits notable computational efficiency. Across the 371 videos comprising our real-world study (cf. Sec. 5.3), the average processing-time/video-duration ratio was computed to be 0.58 with a standard deviation of 0.25, demonstrating faster than real-time processing capability. This contrasts with methods like DiMoDif, which achieve real-time operation (x1.0 video-duration). In addition, AuViRe has 12.1M learnable parameters requiring 1.0 GFLOP for a forward pass of a single video features, and processes ~ 43 FPS (including feature extraction and simultaneous audio processing).

⁸Identical configuration, except the downsampling/upsampling blocks are Transformer encoder blocks with conv./deconv. final layers.

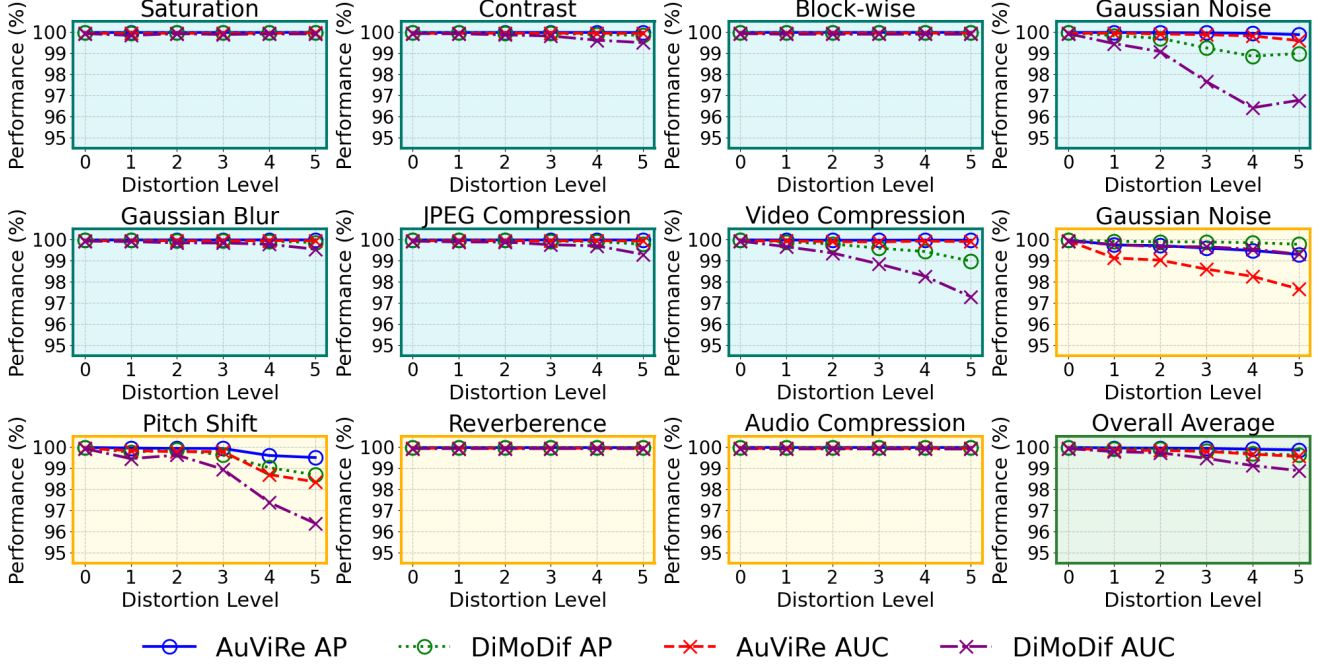


Figure 3. Robustness analysis using visual (cyan plots) and audio (yellow plots) distortions. Overall average robustness is also reported.

Table 9. Ablation analysis on LAV-DF for loss composition (\mathcal{L} comp.), reconstruction-discrepancy encoder input (\mathcal{E} input), reconstruction-discrepancy operation ($\gamma(\zeta, \eta)$), backbone (\mathfrak{B}), and model type (\mathcal{M}). AP@{0.5,0.75,0.95} and AR{100,50,20,10} metrics are reported along with corresponding rank in parenthesis. Last column reports per instance average rank (\bar{R}).

Compon.	Config.	AP@0.5	AP@0.75	AP@0.95	AR@100	AR@50	AR@20	AR@10	\bar{R}	
0	- AuViRe	98.91 (1)	96.03 (1)	46.50 (3)	94.93 (2)	94.56 (3)	93.99 (3)	93.27 (3)	2.2	
1	\mathcal{L} comp.	$\{\mathcal{L}_{focal}, \mathcal{L}_{DIOU}\}$	98.63 (4)	94.33 (12)	43.55 (7)	94.09 (16)	93.59 (16)	92.80 (17)	12.1	
2		$\{\mathcal{L}_{focal}, \mathcal{L}_{s-L1}\}$	98.03 (15)	93.63 (15)	36.36 (14)	94.92 (3)	94.56 (4)	93.99 (4)	93.12 (4)	9.2
3		$\{\mathcal{L}_{focal}, \mathcal{L}_{s-L1}, \mathcal{L}_{rec}\}$	97.97 (17)	93.78 (14)	35.52 (15)	94.82 (6)	94.58 (2)	94.12 (1)	93.28 (2)	9.0
4		$\{\mathcal{L}_{focal}, \mathcal{L}_{DIOU}, \mathcal{L}_{det}\}$	98.47 (9)	94.60 (11)	48.68 (1)	94.13 (15)	93.76 (15)	93.05 (16)	92.17 (16)	11.2
5		$\{\mathcal{L}_{focal}, \mathcal{L}_{s-L1}, \mathcal{L}_{det}\}$	98.08 (14)	91.70 (19)	26.91 (20)	94.72 (9)	94.41 (7)	93.70 (9)	92.68 (10)	13.2
6		$\{\mathcal{L}_{focal}, \mathcal{L}_{DIOU}, \mathcal{L}_{det}, \mathcal{L}_{rec}\}$	98.18 (11)	94.69 (9)	48.65 (2)	94.49 (14)	94.06 (13)	93.40 (13)	92.64 (12)	10.2
7		$\{\mathcal{L}_{focal}, \mathcal{L}_{s-L1}, \mathcal{L}_{det}, \mathcal{L}_{rec}\}$	98.28 (10)	92.89 (16)	32.26 (19)	95.00 (1)	94.64 (1)	93.94 (5)	92.97 (8)	9.4
8	\mathcal{E} input	$\{(a, v)\}$	98.00 (16)	94.70 (8)	38.12 (13)	94.60 (11)	94.23 (10)	93.63 (11)	92.65 (11)	11.5
9		$\{(v, a)\}$	97.65 (19)	93.79 (13)	41.90 (10)	94.60 (10)	94.10 (12)	93.42 (12)	92.61 (13)	12.9
10		$\{(a, a)\}$	95.88 (20)	88.95 (20)	34.78 (16)	93.42 (18)	92.88 (19)	92.07 (19)	91.12 (19)	18.7
11		$\{(v, v)\}$	83.38 (21)	68.00 (21)	13.25 (21)	83.75 (21)	82.42 (21)	80.02 (21)	77.47 (21)	21.0
12		$\{(a, v), (v, a)\}$	98.53 (8)	94.67 (10)	42.52 (9)	94.50 (13)	93.91 (14)	93.07 (14)	92.17 (15)	11.5
13		$\{(a, v), (a, a)\}$	98.59 (7)	94.99 (5)	42.93 (8)	94.58 (12)	94.19 (11)	93.71 (8)	93.08 (6)	8.0
14		$\{(a, v), (v, v)\}$	98.17 (12)	94.88 (6)	43.98 (6)	94.75 (8)	94.39 (8)	93.78 (7)	92.99 (7)	7.8
15		$\{(a, v), (v, a), (a, a)\}$	98.78 (3)	95.31 (3)	44.35 (4)	94.77 (7)	94.28 (9)	93.65 (10)	92.90 (9)	6.0
16		$\{(a, v), (v, a), (v, v)\}$	98.81 (2)	95.57 (2)	41.68 (11)	94.83 (4)	94.43 (6)	93.87 (6)	93.09 (5)	5.1
17		$\{(a, v), (v, a), (a, a), (v, v)\}$	98.62 (5)	94.76 (7)	44.31 (5)	94.82 (5)	94.49 (5)	94.05 (2)	93.49 (1)	4.5
18	$\gamma(\zeta, \eta)$	$\hat{\mathbf{x}}_{(\zeta, \eta)} \cdot \mathbf{x}_\eta$	98.61 (6)	95.14 (4)	39.75 (12)	93.84 (17)	93.54 (17)	93.06 (15)	92.39 (14)	11.5
19	\mathfrak{B}	(Ma et al. 2022) [26]	97.71 (18)	92.11 (17)	33.89 (18)	92.85 (20)	92.41 (20)	91.83 (20)	91.10 (20)	18.8
20	\mathcal{M}	Transformer	98.09 (13)	91.93 (18)	34.55 (17)	93.38 (19)	92.98 (18)	92.27 (18)	91.50 (18)	17.1

6. Conclusions

We introduced AuViRe, a novel method that leverages discrepancies in reconstructed latent space speech represen-

tations to identify deepfakes. AuViRe works by first extracting speech representations from both visual and audio modalities. These are then reconstructed using information from either the same modality or its counterpart. The core

of our approach lies in processing the reconstruction discrepancy with an encoder, which effectively amplifies errors in manipulated video segments. This allows AuViRe to precisely pinpoint deepfake alterations. Our extensive experiments demonstrate that AuViRe not only outperforms state-of-the-art methods but also exhibits strong robustness, generalization, and practical applicability in real-world scenarios. Notably, although not explicitly trained for video-level audio-visual deepfake detection, it surpasses previous state of the art based on its transformed localization output.

7. Acknowledgments

This work is partially funded by the Horizon Europe projects AI4TRUST (GA No. 101070190) and AI-CODE (GA No. 101135437).

References

- [1] Darius Afchar, Vincent Nozick, Junichi Yamagishi, and Isao Echizen. Mesonet: a compact facial video forgery detection network. In *2018 IEEE international workshop on information forensics and security (WIFS)*, pages 1–7. IEEE, 2018. [6](#)
- [2] Jimmy Lei Ba, Jamie Ryan Kiros, and Geoffrey E Hinton. Layer normalization. *arXiv preprint arXiv:1607.06450*, 2016. [3](#)
- [3] Anurag Bagchi, Jazib Mahmood, Dolton Fernandes, and Ravi Kiran Sarvadevabhatla. Hear me out: Fusional approaches for audio augmented temporal action localization. *arXiv preprint arXiv:2106.14118*, 2021. [6](#)
- [4] Navaneeth Bodla, Bharat Singh, Rama Chellappa, and Larry S Davis. Soft-nms—improving object detection with one line of code. In *Proceedings of the IEEE international conference on computer vision*, pages 5561–5569, 2017. [3](#)
- [5] Zhixi Cai, Shreya Ghosh, Aman Pankaj Adatia, Munawar Hayat, Abhinav Dhall, Tom Gedeon, and Kalin Stefanov. Av-deepfake1m: A large-scale llm-driven audio-visual deepfake dataset. In *Proceedings of the 32nd ACM International Conference on Multimedia*, pages 7414–7423, 2024. [1](#), [4](#), [6](#)
- [6] Zhixi Cai, Shreya Ghosh, Abhinav Dhall, Tom Gedeon, Kalin Stefanov, and Munawar Hayat. Glitch in the matrix: A large scale benchmark for content driven audio-visual forgery detection and localization. *Computer Vision and Image Understanding*, 236:103818, 2023. [1](#), [2](#), [4](#), [6](#)
- [7] Zhixi Cai, Kalin Stefanov, Abhinav Dhall, and Munawar Hayat. Do you really mean that? content driven audio-visual deepfake dataset and multimodal method for temporal forgery localization. In *2022 International Conference on Digital Image Computing: Techniques and Applications (DICTA)*, pages 1–10. IEEE, 2022. [1](#), [2](#), [6](#)
- [8] Liang Chen, Yong Zhang, Yibing Song, Lingqiao Liu, and Jue Wang. Self-supervised learning of adversarial example: Towards good generalizations for deepfake detection. In *Proceedings of the IEEE/CVF conference on computer vision and pattern recognition*, pages 18710–18719, 2022. [1](#), [2](#)
- [9] Jongwook Choi, Taehoon Kim, Yonghyun Jeong, Seungryul Baek, and Jongwon Choi. Exploiting style latent flows for generalizing deepfake video detection. In *Proceedings of the IEEE/CVF conference on computer vision and pattern recognition*, pages 1133–1143, 2024. [1](#), [2](#)
- [10] Komal Chugh, Parul Gupta, Abhinav Dhall, and Ramanathan Subramanian. Not made for each other-audio-visual dissonance-based deepfake detection and localization. In *Proceedings of the 28th ACM international conference on multimedia*, pages 439–447, 2020. [1](#), [2](#), [6](#)
- [11] Davide Alessandro Coccomini, Nicola Messina, Claudio Gennaro, and Fabrizio Falchi. Combining efficientnet and vision transformers for video deepfake detection. In *International conference on image analysis and processing*, pages 219–229. Springer, 2022. [6](#)
- [12] Mark De Berg. *Computational geometry: algorithms and applications*. Springer Science & Business Media, 2000. [4](#)
- [13] Brian Dolhansky, Joanna Bitton, Ben Pflaum, Jikuo Lu, Russ Howes, Menglin Wang, and Cristian Canton Ferrer. The deepfake detection challenge (dfdc) dataset. *arXiv preprint arXiv:2006.07397*, 2020. [2](#)
- [14] Joel Frank, Thorsten Eisenhofer, Lea Schönherr, Asja Fischer, Dorothea Kolossa, and Thorsten Holz. Leveraging frequency analysis for deep fake image recognition. In *International conference on machine learning*, pages 3247–3258. PMLR, 2020. [2](#)
- [15] Ross Girshick. Fast r-cnn. In *Proceedings of the IEEE international conference on computer vision*, pages 1440–1448, 2015. [7](#)
- [16] Alexandros Haliassos, Rodrigo Mira, Stavros Petridis, and Maja Pantic. Leveraging real talking faces via self-supervision for robust forgery detection. In *Proceedings of the IEEE/CVF Conference on Computer Vision and Pattern Recognition*, pages 14950–14962, 2022. [6](#)
- [17] Alexandros Haliassos, Konstantinos Vougioukas, Stavros Petridis, and Maja Pantic. Lips don’t lie: A generalisable and robust approach to face forgery detection. In *Proceedings of the IEEE/CVF conference on computer vision and pattern recognition*, pages 5039–5049, 2021. [6](#)
- [18] Yue-Hua Han, Tai-Ming Huang, Kai-Lung Hua, and Jun-Cheng Chen. Towards more general video-based deepfake detection through facial component guided adaptation for foundation model. In *Proceedings of the Computer Vision and Pattern Recognition Conference*, pages 22995–23005, 2025. [1](#), [2](#)
- [19] Hossein Kashiani, Niloufar Alipour Talemi, and Fatemeh Afghah. Freqdebias: Towards generalizable deepfake detection via consistency-driven frequency debiasing. In *Proceedings of the Computer Vision and Pattern Recognition Conference*, pages 8775–8785, 2025. [1](#), [2](#)
- [20] Christos Koutlis and Symeon Papadopoulos. Dimodif: Discourse modality-information differentiation for audio-visual deepfake detection and localization. *arXiv preprint arXiv:2411.10193*, 2024. [2](#), [5](#), [6](#)
- [21] Nicolas Larue, Ngoc-Son Vu, Vitomir Struc, Peter Peer, and Vassilis Christophides. Seeable: Soft discrepancies and bounded contrastive learning for exposing deepfakes. In

- Proceedings of the IEEE/CVF International Conference on Computer Vision*, pages 21011–21021, 2023. 1, 2
- [22] Lingzhi Li, Jianmin Bao, Ting Zhang, Hao Yang, Dong Chen, Fang Wen, and Baining Guo. Face x-ray for more general face forgery detection. In *Proceedings of the IEEE/CVF conference on computer vision and pattern recognition*, pages 5001–5010, 2020. 6
- [23] Yuezun Li, Xin Yang, Pu Sun, Honggang Qi, and Siwei Lyu. Celeb-df: A large-scale challenging dataset for deepfake forensics. In *Proceedings of the IEEE/CVF conference on computer vision and pattern recognition*, pages 3207–3216, 2020. 2
- [24] Tsung-Yi Lin, Priya Goyal, Ross Girshick, Kaiming He, and Piotr Dollár. Focal loss for dense object detection. In *Proceedings of the IEEE international conference on computer vision*, pages 2980–2988, 2017. 3
- [25] Yuzhen Lin, Wentang Song, Bin Li, Yuezun Li, Jiangqun Ni, Han Chen, and Qiushi Li. Fake it till you make it: Curricular dynamic forgery augmentations towards general deepfake detection. In *European Conference on Computer Vision*, pages 104–122. Springer, 2024. 1
- [26] Pingchuan Ma, Stavros Petridis, and Maja Pantic. Visual speech recognition for multiple languages in the wild. *Nature Machine Intelligence*, 4(11):930–939, 2022. 7, 8
- [27] Rami Mubarak, Tariq Alsbou, Omar Alshaikh, Isa Inuwa-Dutse, Saad Khan, and Simon Parkinson. A survey on the detection and impacts of deepfakes in visual, audio, and textual formats. *Ieee Access*, 11:144497–144529, 2023. 1
- [28] Yuyang Qian, Guojun Yin, Lu Sheng, Zixuan Chen, and Jing Shao. Thinking in frequency: Face forgery detection by mining frequency-aware clues. In *European conference on computer vision*, pages 86–103. Springer, 2020. 6
- [29] Andreas Rossler, Davide Cozzolino, Luisa Verdoliva, Christian Riess, Justus Thies, and Matthias Nießner. Faceforensics++: Learning to detect manipulated facial images. In *Proceedings of the IEEE/CVF international conference on computer vision*, pages 1–11, 2019. 2
- [30] Bowen Shi, Wei-Ning Hsu, Kushal Lakhota, and Abdelrahman Mohamed. Learning audio-visual speech representation by masked multimodal cluster prediction. In *International Conference on Learning Representations*, 2022. 1, 3, 7
- [31] Kaede Shiohara and Toshihiko Yamasaki. Detecting deepfakes with self-blended images. In *Proceedings of the IEEE/CVF Conference on Computer Vision and Pattern Recognition*, pages 18720–18729, 2022. 1, 2, 6
- [32] Chao Shuai, Jieming Zhong, Shuang Wu, Feng Lin, Zhibo Wang, Zhongjie Ba, Zhenguang Liu, Lorenzo Cavallaro, and Kui Ren. Locate and verify: A two-stream network for improved deepfake detection. In *Proceedings of the 31st ACM International Conference on Multimedia*, pages 7131–7142, 2023. 1
- [33] Limin Wang, Bingkun Huang, Zhiyu Zhao, Zhan Tong, Yinan He, Yi Wang, Yali Wang, and Yu Qiao. Videomae v2: Scaling video masked autoencoders with dual masking. In *Proceedings of the IEEE/CVF Conference on Computer Vision and Pattern Recognition*, pages 14549–14560, 2023. 6
- [34] Yuting Xu, Jian Liang, Gengyun Jia, Ziming Yang, Yanhao Zhang, and Ran He. Tall: Thumbnail layout for deepfake video detection. In *Proceedings of the IEEE/CVF international conference on computer vision*, pages 22658–22668, 2023. 1
- [35] Zhiyuan Yan, Yandan Zhao, Shen Chen, Mingyi Guo, Xinghe Fu, Taiping Yao, Shouhong Ding, Yunsheng Wu, and Li Yuan. Generalizing deepfake video detection with plug-and-play: Video-level blending and spatiotemporal adapter tuning. In *Proceedings of the Computer Vision and Pattern Recognition Conference*, pages 12615–12625, 2025. 1
- [36] Kelu Yao, Jin Wang, Boyu Diao, and Chao Li. Towards understanding the generalization of deepfake detectors from a game-theoretical view. In *Proceedings of the IEEE/CVF International Conference on Computer Vision*, pages 2031–2041, 2023. 1
- [37] Chen-Lin Zhang, Jianxin Wu, and Yin Li. Actionformer: Localizing moments of actions with transformers. In *European Conference on Computer Vision*, pages 492–510. Springer, 2022. 6
- [38] Hang Zhang, Xin Li, and Lidong Bing. Video-llama: An instruction-tuned audio-visual language model for video understanding. In *Proceedings of the 2023 Conference on Empirical Methods in Natural Language Processing: System Demonstrations*, pages 543–553, 2023. 6
- [39] Rui Zhang, Hongxia Wang, Mingshan Du, Hanqing Liu, Yang Zhou, and Qiang Zeng. Ummaformer: A universal multimodal-adaptive transformer framework for temporal forgery localization. In *Proceedings of the 31st ACM International Conference on Multimedia*, pages 8749–8759, 2023. 1, 2, 6
- [40] Hanqing Zhao, Wenbo Zhou, Dongdong Chen, Tianyi Wei, Weiming Zhang, and Nenghai Yu. Multi-attentional deepfake detection. In *Proceedings of the IEEE/CVF conference on computer vision and pattern recognition*, pages 2185–2194, 2021. 1, 2
- [41] Zhaohui Zheng, Ping Wang, Wei Liu, Jinze Li, Rongguang Ye, and Dongwei Ren. Distance-iou loss: Faster and better learning for bounding box regression. In *Proceedings of the AAAI conference on artificial intelligence*, volume 34, pages 12993–13000, 2020. 3

A. Hyperparameter tuning

Fig. 4 presents our hyperparameter tuning experimental results. These are obtained by training and evaluating AuViRe on LAV-DF on a grid of 36 experiments defined by $d_a \in \{32, 64, 128, 256\}$, $l_{down}^r = l_{up}^r \in \{1, 2, 3\}$, and $l_{retain}^e = l_{down}^e \in \{1, 2, 3\}$. High AP is achieved with $d_a \in \{32, 64\}$ but with lower AR scores. $d_a \in \{128, 256\}$ strike a balance between AP and AR with the best configuration obtaining average rank 6.7 defined by $d_a = 128$, $l_{down}^r = l_{up}^r = 3$, $l_{retain}^e = l_{down}^e = 2$. The same analysis on AV-Deepfake1M (validation set) is illustrated in Fig. 5.

B. Robustness

Tab. 10 reports average backbone \mathfrak{B} feature similarity among original and distorted versions of the same LAV-DF samples, showcasing its high resilience that contributes to AuViRe’s robustness.

C. Generalization

Tabs. 11 and 12 show cross-dataset generalization performance for DFD and TFL. Trained on AV-Deepfake1M, a set ten times larger with higher quality generated content, the model achieves strong performance on LAV-DF, with 93.33 AUC (+7.03 compared to DiMoDif) and 43.3 AP@0.75 (+17.1 compared to DiMoDif). Trained on LAV-DF AuViRe performs on par to DiMoDif (-1.51 AUC, +2.1 AP@0.75). The failure of both models at 90/95% IoU is attributed to the x2 larger forged segments of LAV-DF vs. AV-Deepfake1M.

D. Threshold Calibration

Fig. 6, presents a systematic calibration analysis using the real-world data indicating 0.01 as Ψ_m ’s optimal probability threshold θ .

E. Real-world performance drop: Examples

Figure 7 provides further qualitative examples pinpointing the most prominent contributing factors to the performance drop from a controlled to the real-world uncontrolled environment.

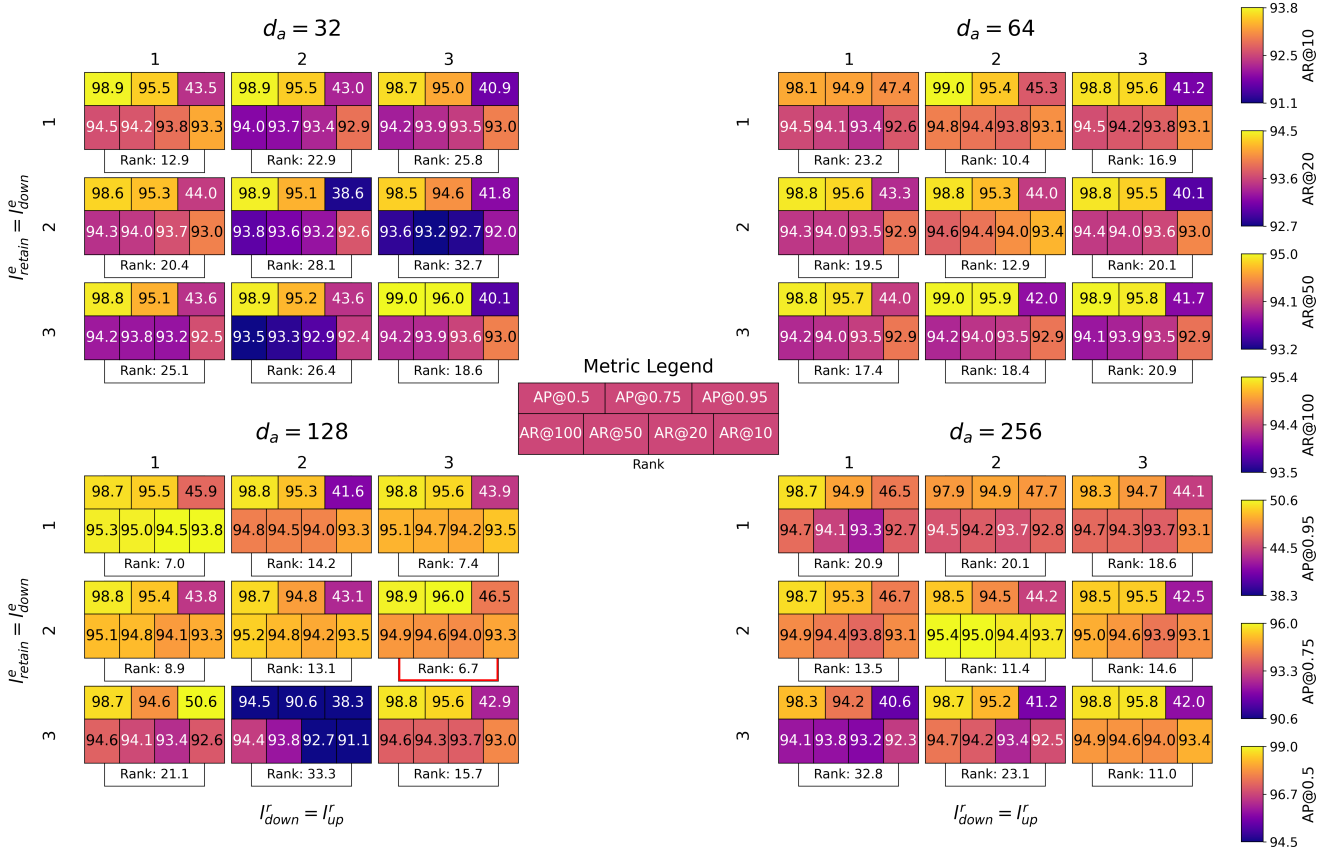


Figure 4. Hyperparameter grid results on LAV-DF. Best rank is highlighted with red.

Table 10. Average cosine similarity of \mathfrak{B} extracted features, between original and distorted versions of 1,000 LAV-DF unseen samples.

Modality	Distortion	Level 1	Level 2	Level 3	Level 4	Level 5
Visual	Color Saturation	0.96 ± 0.05	0.96 ± 0.05	0.97 ± 0.05	0.96 ± 0.05	0.97 ± 0.05
	Color Contrast	0.95 ± 0.05	0.93 ± 0.06	0.89 ± 0.08	0.83 ± 0.10	0.73 ± 0.10
	Block-wise	0.96 ± 0.04	0.96 ± 0.04	0.94 ± 0.06	0.92 ± 0.08	0.88 ± 0.11
	Gaussian Noise	0.87 ± 0.08	0.79 ± 0.10	0.64 ± 0.13	0.48 ± 0.16	0.09 ± 0.10
	Gaussian Blur	0.94 ± 0.06	0.92 ± 0.08	0.86 ± 0.10	0.79 ± 0.11	0.71 ± 0.13
	JPEG	0.96 ± 0.05	0.94 ± 0.07	0.90 ± 0.08	0.84 ± 0.09	0.75 ± 0.10
	Video Compression	0.89 ± 0.06	0.85 ± 0.06	0.77 ± 0.09	0.67 ± 0.09	0.59 ± 0.10
Audio	Gaussian Noise	0.81 ± 0.07	0.73 ± 0.09	0.66 ± 0.10	0.58 ± 0.11	0.49 ± 0.11
	Pitch Shift	0.88 ± 0.04	0.67 ± 0.18	0.49 ± 0.25	0.35 ± 0.22	0.26 ± 0.20
	Reverberence	1.00 ± 0.03	1.00 ± 0.03	1.00 ± 0.04	0.99 ± 0.04	0.99 ± 0.06
	Audio Compression	0.88 ± 0.17	0.60 ± 0.10	0.51 ± 0.11	0.56 ± 0.19	0.99 ± 0.06

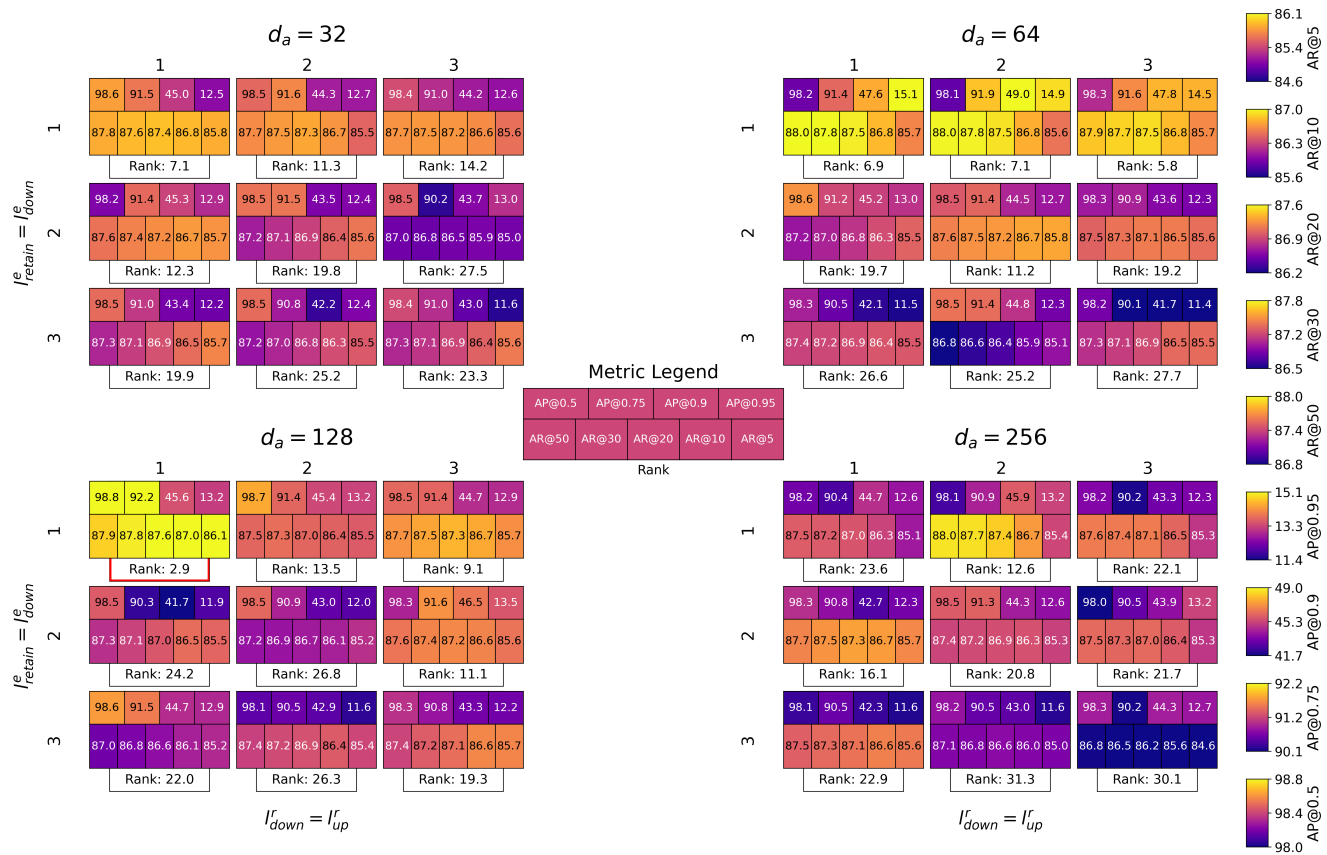


Figure 5. Hyperparameter grid results on AV-Deepfake1M. Best rank is highlighted with red.

Table 11. Generalization performance on Deepfake Detection task.

Trained on	Model	Tested on			
		LAV-DF		AVDIM	
		AP	AUC	AP	AUC
AVDIM	DiMoDif	94.98	86.30	-	96.30
	AuViRe	97.66	93.33	-	99.78
LAV-DF	DiMoDif	99.94	99.84	-	67.21
	AuViRe	99.98	99.94	-	65.70

Table 12. Generalization performance on Temporal Forgery Localization task.

Trained on	Tested on	Method	AP				AR					
			@0.5	@0.75	@0.9	@0.95	@100	@50	@30	@20	@10	@5
AVDIM	LAV-DF	DiMoDif	59.8	26.2	2.3	0.2	75.3	72.3	69.7	67.3	62.5	56.2
		AuViRe	53.8	43.3	13.9	0.9	78.0	76.5	75.2	74.1	71.4	66.8
LAV-DF	AVDIM	DiMoDif	15.9	4.3	0.3	0.02	-	28.9	27.3	25.7	22.5	19.1
		AuViRe	14.7	6.4	0.6	0.05	-	29.3	26.6	24.6	21.3	18.2

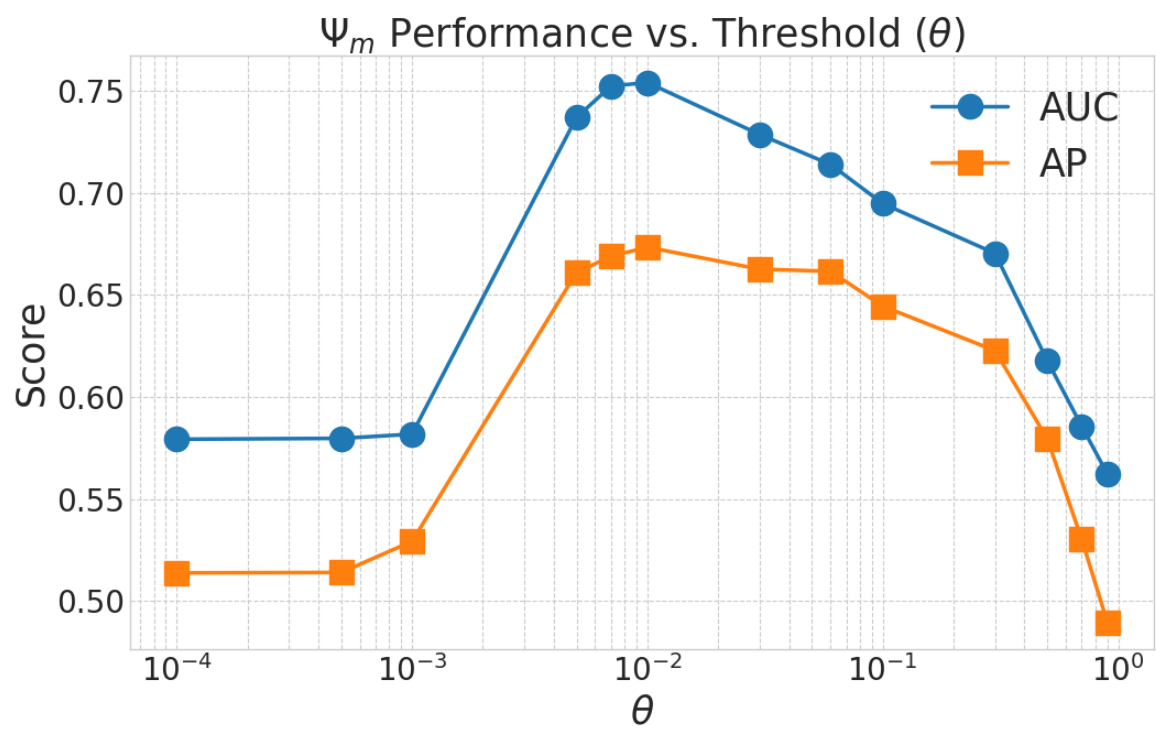


Figure 6. Calibration of Ψ_m 's θ parameter.

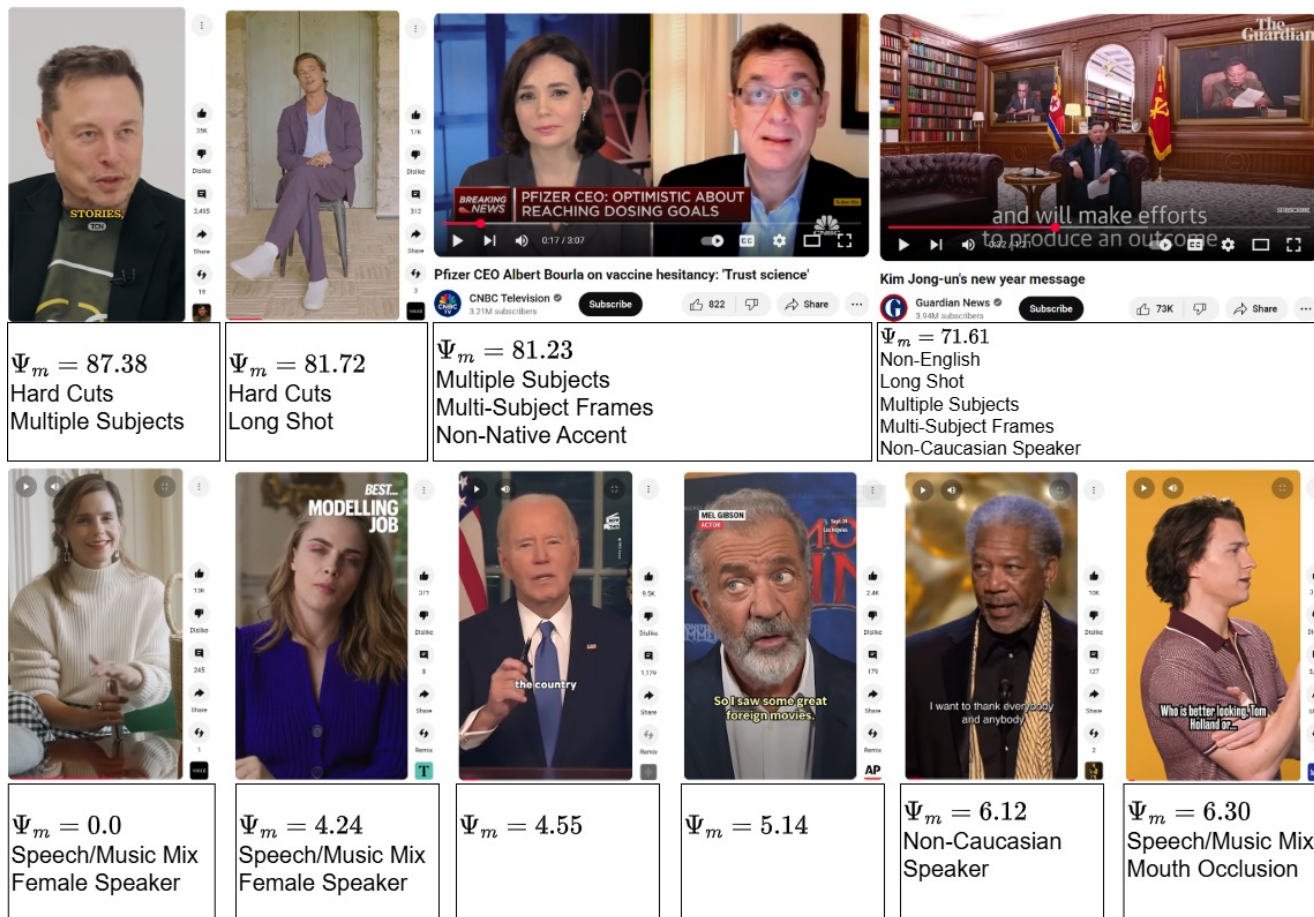


Figure 7. Examples of erroneously (upper panel; 1: <https://www.youtube.com/shorts/c15HhmtfI5w>, 2: <https://www.youtube.com/shorts/cqkYUfOf9c>, 3: https://www.youtube.com/watch?v=P606FqYYImk&ab_channel=CNBCTelevision, 4: <https://www.youtube.com/watch?v=YLWqqDVWsXo>) and correctly (bottom panel; 1: <https://www.youtube.com/shorts/ciSd7M3lAco>, 2: https://www.youtube.com/shorts/kyf_eCCc5qU, 3: <https://www.youtube.com/shorts/EVQo--qKQAI>, 4: https://www.youtube.com/shorts/dvfn3WD1_A8, 5: <https://www.youtube.com/shorts/JW4FT8RVJ88>, 6: <https://www.youtube.com/shorts/gH96b2U293Y>) classified **real** samples.